OPTIMIZATION OF PZT BASED THIN FILMS AND PIEZOELECTRIC MICROMACHINED ULTRASONIC TRANSDUCERS (pMUTs)

By

ABHISHEK DALAKOTI

A thesis submitted in partial fulfillment of
the requirements for the degree of

MASTERS OF SCIENCE IN MATERIALS SCIENCE
AND ENGINEERING

WASHINGTON STATE UNIVERSITY
School of Mechanical and Materials Engineering

DECEMBER 2005

To the Faculty of Washington State University:

The members of the Committee appointed to examine the thesis of Abhishek Dalakoti find it satisfactory and recommend that it be accepted.

_____
Chair

_____

_____

ACKNOWLEDGEMENT

I would like to extend special thanks to all those who invested their time, effort, expertise and perspective to help me guide through out my research work as a Master's student at WSU. First, let me thank Dr. Susmita Bose, my advisor, for providing me a great opportunity to work on this project. She was always there, throughout the research work to provide the indispensable guidance and the positive critical feedback. The amount of time spent by her, not only for my research work, but also in introducing me to the new university environment and in providing the necessary moral support is sincerely appreciated. I would also like to take the pleasure to acknowledge Dr. Amit Bandyopadhyay, co-advisor, who helped me in understanding the intricacies of the subject. His insight and expertise in this field has immensely helped and motivated me to present this research work in its present form. I would also like to thank Dr. Grant Norton, committee member, for his continual support and encouragement. His knowledge and considerate nature need no introduction and I am privileged to be benefited by his know-how during his lectures and the course of this project.

I would also like to thank former graduate students, Mr. Todd Myers, Mr. Parag Banerjee and Mr. Firas Akasheh, whose initial work in this field has made the things a lot easier to understand and for providing a foundation to start from. Mr. Hongsoo Choi, current graduate student, is also appreciated for his support regarding mask designing, sputtering experiments and frequent important conversations.

I would also like to thank Mr. Mark Fuller and Mr. Steve Brown for introducing me to various machines and microfabrication techniques in the Clean Room.

I would also like to acknowledge my current batch mates Mr. Sheldon Bernard, Mr. Ashis Banerjee, Mrs. Kakoli Das, Mr Young Jin Choi, Mr. Zach Seeley and Mr. Harpreet Singh for the wonderful time I had with them during the last two years.

And finally, I would like to express sincere gratitude to my parents and my brother, Animesh, who have encouraged me throughout my undergraduate and graduate studies.

OPTIMIZATION OF PZT BASED THIN FILMS AND PIEZOELECTRIC MICROMACHINED ULTRASONIC TRANSDUCERS (pMUTs)

Abstract

By Abhishek Dalakoti
Washington State University
December 2005

Chair: Susmita Bose

This thesis elaborates the research work done to achieve piezoelectric micromachined ultrasonic transducers (pMUTs) devices for medical imaging with better properties in terms of coupling efficiency, reliability and bandwidth. The objective was approached with optimizing materials and design parameters. Lead zirconate titanate (PZT) based piezoelectric thin films were used as the active element for these devices and the PZT material properties such as polarization values, dielectric constant, ferroelectric fatigue resistance, sintering temperature and others, were further improved by doping with zinc, strontium and yttrium. Wherein, strontium showed improved dielectric and polarization values, zinc showed lower sintering temperature and higher polarization values and yttrium resulted in improved ferroelectric fatigue resistance of the film. Finally, the doped PZT composition was optimized as 52/48 PZT + 2%Zn + 2%Sr for next step, the device fabrication. Flexural mode of vibration was used to create frequencies in the range of 1-4 MHz using PZT coated silicon membrane. Two independent designs X and Y were separately evaluated to understand the effect of membrane dimension, top gold electrode dimension and effective membrane area

covered by it on the resonance frequency and coupling coefficient. Doped optimized PZT solution was used as the active material for device fabrication. Variation in the resonance frequency as a function of membrane dimension for both the designs was established. Optimum position and width of top gold electrode for design X corresponding to different membrane dimension was identified and an expansion of 10μm beyond membrane width was found to be most effective. For design Y also gold electrode of (+) 10μm gave better results then (-) 10μm. Efficiency decreased on increasing gap width from 20μm to 30μm for design Y. Fabricated device was also characterized by running hysteresis curve, ferroelectric fatigue and FESEM pictures of the cross section and back side of the membrane.

TABLE OF CONTENTS

Page

LIST OF TABLES

LIST OF FIGURES

CHAPTER ONE

INTRODUCTION

1.1 Motivation

Microelectromechanical systems (MEMS) based ultrasonic medical imaging devices are gaining attention among the researchers because of the possibilities to solve long standing problems and innovate new products. The tremendous growth observed in this field is primarily due to advancement in the integrated circuit (IC) industry. For the last few years, piezoelectric micromachined ultrasonic transducers (pMUTs) are investigated for fabrication of high frequency acoustic imaging devices to improve resolution and frequency limitations of presently available and relatively less effective bulk transducers. One critical research area associated with this field focuses on miniaturizing and exploring materials and fabrication techniques for forward looking endoscopes as a substitution for presently available side looking devices. To develop such devices it is important to understand and optimize both material and design issues for pMUTs.

Swartz et al. [1] was the first to produce silicon based integrated ultrasonic transducer, POSFET, which was a combination of PVDF (polyvinylidene fluoride) transducer with MOSFET (metal-oxide semiconductor field-effect transducer) input amplifier. In 1950, when PZT based piezoelectric ceramic was invented, it soon became popular because of exceptionally high piezoelectric properties. PZT is now the most commonly used active element of any ultrasonic transducer. But problems associated with their fabrication, cost, reliability and low frequency range available for the device to operate (bandwidth) in the bulk transducers have forced researchers to look for better

alternatives in the form of lead zirconate titanate (PZT) thin films. Bulk piezoelectric transducers utilizing thickness mode of vibration for high frequency, require accurate dicing to the order of 50μm in order to generate ultrasonic frequencies in the range of 2-50 MHz. The complexity of the fabrication process are further enhanced by the necessity of an impedance matching layer for output energy maximization and a suitable backing material for providing support and damping effect to reduce ringing. A single bulk transducer, therefore, require costly and accurately designed active element, matching layer and backing material. The situation becomes more serious due to the narrow bandwidth, typically 70%, available with these devices. Another critical issue associated with these bulk transducers is the reliability, presence of fast alternating electric field distorts the reorientation of electrical domains inside the active element (ferroelectric fatigue), thereby, reducing the polarization values and affecting the efficiency of the device. The novel thin film based transducers seems to answer these problems. Given the fact that IC technology is so well developed, about 50 transducers can be easily fabricated in a single three inch silicon wafer. Modulation of the resonance frequency becomes much easier, since it utilizes the flexural mode of vibration, wherein, the width of the vibrating membrane is an important dimension, as against to the thickness and can be easily adjusted according to the frequency requirements. In absence of matching layer and backing material these devices are expected to have a much wider bandwidth, typically100%, then their bulk counterpart. Additionally, the ferroelectric fatigue is much more suppressed due to the presence of fewer domain regions that needs to be reoriented in a thin film. The resistance to the fatigue can be further improved by careful addition of selected dopants. However, micromachined transducers suffer from low efficiency due to

thin (1-2μm) active piezoelectric layer available as against to 50-100μm in the case of bulk transducers. Improving the material properties and optimizing the design criteria can provide a solution to low efficiency due to the presence of less active element.

One of the current challenges among the researchers in the field of ultrasonic imaging is the fabrication of 2D arrays of transducers to obtain 3D body imaging along with high scanning frequencies and coupling coefficient (efficiency of the energy conversion in the component), using low voltage stimulation [2]. Moreover, 3D ultrasound can prove to be a cheaper solution to the costly CT and MRI imaging available today. Although, it would require complex signal processing and image development techniques, but at the same time improved active element of the transducer and the design of these transducer elements can significantly influence the overall performance of these 3D imaging devices.

In brief, the driving force for the research work discussed in this thesis can be summarized as the call for efficient pMUT devices for medical imaging. Need for cost effective devices with high coupling coefficient and broad inherent bandwidth which can match acoustic impedance of human body exist today. Understanding the effects of various design and material parameters to tailor transducer performance is the main focus of this research.

1.2 Research Objective

Frequency required for medical imaging inside the body is limited to the range of 2-30MHz. A higher frequency enables better resolution but at the cost of depth of penetration. Frequencies in the range of 30-70MHz are used for surface imaging with microscopic resolution as in the case of imaging anterior chamber of the eye [3].

However, most conventional ultrasonic medical imaging transducers operate in the range of 2-15MHz. Problems associated with these conventional bulk transducers were introduced in the previous section and thin film based transducers were suggested as the best alternative. In order to fabricate these high quality micromachined thin film transducers, it is imperative to first of all improve the material characteristics, so that power obtained from a piezoelectric layer of 1-2μm is good enough to produce intense ultrasonic waves for a given signal. For this reason, current research work focuses on PZT based thin films, because of their exceptional piezoelectric properties. Of all the possible compositions $Pb(Zr_{0.52}Ti_{0.48})O_3$ was extensively studied along with dopants addition, since it lies at the morphotrophic phase boundary (MPB) and hence, associated with peaks in piezoelectric coupling, compliance and dielectric permittivity. Zn, Sr and Y were meticulously added to this composition to improve polarization values, dielectric constant and resistance to fatigue. These thin film transducers are relatively new to the research field; therefore, there is an insufficient understanding of the design issues, which leads to lack of confidence on any data obtained. This research work investigates the effect of various design parameters as an effort to improve the efficiency and understand its influence on the resonance frequency of the device. Two different designs were proposed and the dimension of membrane and electrode were varied to optimize them according to efficiency and frequency requirements.

In brief, the goal of this research was to improve the existing pMUTs by exploring better materials for thin film piezoelectric actuation and understanding the effect of various design parameters on the overall performance of the device. Variables

both from material and design point of view were systematically analyzed and tested to evaluate their impact on device performance.

1.3 Outline of Research

The current research work is presented over 3 chapters. Chapter two investigates the material aspect and explores the effect of zinc, strontium and yttrium on ferroelectric properties of PZT based thin films. MEMS devices using piezoelectric effect of PZT thin films are preferred due to their low electrical noise in sensing application, high force output in actuation applications and high sensitivity [4-5]. Since the PZT thin films form the active element of these ultrasonic devices, any further improvement in the properties of these films will automatically improve the performance of the device. Keeping this in mind, effect of individual dopant was first established in terms of remnant and saturation polarization, coercive field, ferroelectric fatigue, dielectric constant and crystallization temperatures. This was followed by optimizing the combination of these dopants to further improve the properties. Details of design of experimentation and final optimized composition achieved are discussed in chapter two.

Chapter three focuses on the comprehension of various design parameters of pMUTs. Flexural mode of vibration i.e., k_{31} is used instead of thickness mode to generate desired frequency, wherein, the electric field is applied across the thickness, the 3 direction, resulting in the vertical bending of the membrane due to lateral strain along 1 direction. Initial FEM modeling reported previously by our research group has helped to narrow down on the range for various parameters. Current research work analyzes the effect of dimensions of vibrating membrane and design and dimension of top gold electrode using optimized PZT thin films. Corel-Draw was used to design these

membranes and top gold electrode. Various parameters partly constricted by FEM modeling were then scanned methodically to understand their individual effect. Details of the design and results obtained are explained in chapter three.

1.4 Reference

1. R.G. Swartz and J.D. Plummer, Integrated Silicon PVDF Acoustic Transducer Arrays, IEEE Transactions Electron Devices, Vol. ED-26, No. 12, pp. 1921-1931, 1979

2 K. Lefki and G.J.M. Dormans, Measurement of Piezoelectric Coefficients of Ferroelectric Thin Films, Journal of Applied Physics, 76, 1764-1767 (1994)

3 I. Ladabaum, X. Jin, H.T. Soh, A. Atalar, Surface Micromachined Capacitive Ultrasonic Transducers, IEEE Transactions on Ultrasonics, Ferroelectrics and Frequency Control, Vol. 45, No. 3, (1998) 678

4 A. Schroth, C. Lee, S. Matsmuto and R. Maeda, Application of Sol-gel Deposited Thin Film for Actuation of 1D and 2D Scanners, Sensors and Actuators 73 (1999) 144-152

5 G.R. Lockwood, D.H. Turnbull, D.A. Christopher and F.S. Foster, Beyond 30MHz: Application of High Frequency Ultrasonic Imaging, IEEE Engineering in Medicine and Biology, Vol. 15, No. 6, pp. 60-71, 1996

6 D.L. Polla, L.F. Francis, Ferroelectric Thin Films in Microelectrcomechanical Systems Applications, MRS Bulletin 21(7): 59-65, 1996

7 C.C. Hsueh, T. Tamagawa, C. Ye, A. Helgesona and D.L. Polla, Sol-gel Derived Ferroelectirc Thin Films in Silicon Micromachining, Integerate Ferroelectrics, Vol. 3, pp. 21-32, 1993

CHAPTER TWO

Effect of Zn, Sr and Y addition on PZT thin films

Abhishek Dalakoti, Amit Bandyopadhyay and Susmita Bose

School of Mechanical and Materials Engineering

Washington State University

Pullman, WA 99164

2.1 Abstract

We have investigated methods to improve piezoelectric properties of PZT based thin films, which is a key component of piezoelectric micromachined ultrasonic transducers (pMUTs). As pMUTs are driven by a thin piezoelectric layer on a Si membrane, improvement of piezoelectric properties of thin films can significantly increase their efficiency. We have used Zn, Sr and Y doping on PZT based thin films along the morphotrophic phase boundary (MPB) composition to increase its piezoelectric properties. Results obtained were then extended to compositions both sides of the MPB. Sol-gel method was used to make precursor solutions and then spin coated on Pt(100)/Ti/SiO_2/Si substrate for making the PZT thin films. It was found that Zn and Sr together had the most significant effect on properties of PZT thin films in which a saturation polarization of 108 μC/cm^2 and remnant polarization of 54 μC/cm^2 was achieved.

2.2 Introduction

Piezoelectric micromachined ultrasonic transducers (pMUTs) are an example of application of MEMS technology to ultrasound generation and detection, which is expected to offer many advantages over conventional ultrasonic transducers [1-2].

Unfortunately, pMUTs typically show a 3 to 5% efficiency for “31” or flexural mode designs compared to >30% efficiency for conventional "dice and fill" based bulk transducers [1]. Fabrication of high efficiency pMUTs require clear understanding and maximization of properties of materials used and the designs proposed. Various parameters that need to be optimized are dielectric constant, polarization values, ferroelectric fatigue, resonance frequency, coupling coefficient and others for a better transducer device for 2D and 3D medical imaging. Some of these values are actually interrelated, such as dielectric constant, polarization values and coupling coefficient. Lead zirconate titanate (PZT) based thin films were used in our study due to their excellent piezoelectric properties. Of the various possible compositions, ferroelectric properties at the MPB are maximized due to the co-existence of rhombohedral and tetragonal phases [3]. Easy modulation of various ferroelectric properties by cation doping gives an additional advantage to these thin films [4-6]. We have developed PZT based thin films to be used in pMUTs focusing on increasing remnant and saturation polarization, improving ferroelectric fatigue resistance, and dielectric constant, while decreasing coercive field and reducing crystallization temperature using Zn, Sr and Y as ‘A’ and ‘B’ site cation doping. Addition of Y into ‘A’ site was done to reduce oxygen vacancies and improve fatigue resistance. Sr was added into ‘A’ site to increase remnant and saturation polarization via tailored grain orientation and Zn was added into ‘B’ site to reduce crystallization temperature. Combined effects of all these dopants were also evaluated for thin PZT films of thickness less than 1 micron.

2.3 Experimental Procedure

PZT based thin film having composition as $\{Pb_{1-x-y}\ Sr_x Y_y\ [(Zr_{.52}\ Ti_{.48})_{1-z}\ Zn_z]\ O_3\}$, with different values for x, y and z were fabricated. 50 ml, 0.5M metallorganic precursor solution was prepared via sol-gel method using 2-methoxy ethanol (2MOE) as solvent and lead acetate tri-hydrate, titanium isopropoxide (97%), zirconium n-propoxide (70% w/w in propanol), strontium isopropoxide (97%), yttrium isopropoxide (95%) and zinc acetate as starting materials. All the chemicals were purchased from Alfa Aesar, MA, and used without any further purification. Stoichiometric amount of lead acetate tri-hydrate and zinc acetate were dissolved in 2MOE. 10-mol% excess lead was added to this solution to compensate for the lead-loss due to volatization during sintering. This solution was distilled at 125^0C for 2h to remove the water of crystallization. Zirconium n-propoxide and titanium isopropoxide were then added along with the dopants viz. strontium isopropoxide and yttrium isopropoxide in a moisture controlled glove box, in desired amount to the above distilled solution. The solution was then refluxed at 125^0C for 3h to achieve a homogeneous precursor solution. Strontium isopropoxide and yttrium isopropoxide could not be added to the solution during distillation because of their higher susceptibility to oxidation and, therefore, were later added during the refluxing step. However, zinc acetate was added during distillation.

The solution was spin coated on platinized silicon substrate at 4000 rpm for 12 sec. After each layer, the film was heated for 5 minutes separately on hot plates maintained at 125^0C and 325^0C. This process was repeated up to four layers. Final sintering was then carried out in a furnace maintained at 700^0C for 15 minutes. In case of eight or twelve layer films, intermediate sintering at 600^0C for 15 minutes was carried out

after every four layers, before depositing another four-layer film sequence, followed by final sintering at 700^0C for 15 minutes.

For electrical characterization, gold pads (120 nm thick and .0785 μm^2 in area) were sputtered on top of the films. For phase analysis, X-ray diffraction studies were performed using a Philips PW 3040/00 X'pert MPD system with Co-K_a radiation and a Ni-filter over a 2? range of 20^0 to 70^0. Ferroelectric properties were characterized using a Precision Workstation (Radiant Technologies, Albuquerque, NM). All ferroelectric fatigue tests were carried out at 1 MHz and 3V. Hysteresis measurements were taken with a period of 5 ms and a delay of 10 ms between preset loop and measurement loop.

2.4 Results and Discussion

A base line was first established with undoped PZT compositions Pb (Zr_x Ti_{1-x}) O_3, with Zr/Ti ratio of 60/40, 52/48 and 40/60. Most of the measurements were then made with Zn, Sr, and Y addition at the Zr/Ti ratio of 52/48 or MPB composition and using eight-layer films, which had an average thickness of 600 nm. XRD pattern of all the samples showed peaks to confirm the presence of only perovskite phase, and no pyrochlore phase was detected. Most of the ferroelectric fatigue degradation was noticed after 10^8 cycles at 1MHz. Therefore, film qualities were compared after 10^8 and 10^9 cycles.

It was found that with increasing Zn content from 1 to 2 mol% in 52/48 PZT composition, there was an apparent increase in the saturation polarization (Ps) from 50 to 72 $\mu C/cm^2$, as shown in figure 2.1. The coercive field (Ec) and the remnant polarization (Pr) values remained almost the same, 100KV/cm and 27 $\mu C/cm^2$ respectively. As shown in figure 2.2, (110), (111) and (200) perovskite peaks were well developed in the

XRD pattern for the 2 mol% Zn doped 52/48 PZT film sintered at 650^0C. XRD result confirmed that crystallization was complete by 650^0C and ferroelectric properties were similar to 700^0C sintered films. Similar results were reported on bulk PZT due to ZnO addition in which sintering temperature was dropped by 400 ^{o}C [7]. Ferroelectric fatigue degradation in 2-mol% Zn doped thin films was rapid with the film losing 90% of remnant polarization value within 10^9 cycles. A slight decrease, from 4400 to 3800, in the effective dielectric constant (K) value was also observed on increasing Zn from 1 to 2-mol%. These results are tabulated in Table 2.1. This effective K was calculated from the slope of the initial linear part of the hysteresis plot.

With increase in Sr concentration from 1 to 2 mol%, significant improvement in both remnant (Pr) and saturation (Ps) polarization values were observed as shown in figure 2.3. Pr increased from 23 to 33 μC/cm^2 and Ps increased from 44 to 69 μC/cm^2. Effective K with Sr addition increased significantly compared to Zn addition, with values > 6000. However, increase in Sr content from 1 to 2 mol% didn't change K significantly.

A higher K value with the addition of Sr can be explained from the phase formation. It is known that K, coupling factor and piezoelectric constant have their maximum values when compositions are shifted to the tetragonal side of MPB [3]. If we compare the intensity pattern of the XRD of 2% Zn and 2% Sr doped PZT composition, as shown in figure 2.2, we find that the intensity ratio of (111)/(200) is almost 20% greater for 2% Sr doped PZT, which makes it more tetragonal than the 2% Zn doped PZT composition. Sr doped film showed better fatigue resistance, compared to 2% Zn and retained ~ 36% of Pr after 10^9 cycles as opposed to 10% after 10^9 cycles for Zn doped.

However, the films became dielectrically hard with increasing Sr content, as Ec increased from 62 to 136 KV/cm.

Next, various combination of Zn and Sr were tested with and without a donor cation, Y^{+3}, to reduce oxygen vacancies created by substitution of Ti^{+4}/Zr^{+4} site with Zn^{+2}. 2-mol% Y^{+3} with 52/48 PZT thin film was tested. Although these films showed good fatigue response, Pr, Ps and K values were lower compared to un-doped 52/48 PZT. Exceptional properties were obtained for 52/48 PZT with 2%Sr + 2%Zn addition, shown in figure 2.3. The film showed a Ps of 108 μC/cm^2, a Pr of 54 μC/cm^2 and a K of 5000. There was relatively less degradation in the polarization values as compared to 2-mol% Zn doped film. 32% of the Pr value was retained as compared to 10% for Zn doped, when it was tested for hysteresis after running the fatigue test for 10^9 cycles. I-V test on the film showed a uniform resistance of $1.95x10^8$O making it a good capacitive film. This dopant combination (2%Zn+2%Sr) was then tried with 40/60 and 60/40 PZT compositions. It was found that polarization values were lower compared to 52/48 PZT.

Zn addition to the thin film improved saturation polarization and reduced sintering temperature. This was also accompanied by an increase in ferroelectric fatigue degradation and reduced dielectric constant.

$$ZnO + ZrO_2/TiO_2 \rightarrow Zn_{Zr}^{''}/Zn_{Ti}^{''} + O_O^{\ x} + V_O^{\cdot\cdot} \qquad (1)$$

On the basis of size ratio as shown in Table 2.2, Zn^{+2} is expected to substitute Ti^{+4}/Zr^{+4} ions. It is clear from Equation 1, that Zn substitution will cause an increase in oxygen vacancy concentration within the film. These oxygen vacancies get collected at the low energy domain boundaries, thereby, making the domain walls difficult to reorient under an applied alternating field [8-9]. A low sintering temperature with the Zn addition can

either be due to the formation of some low melting liquid phase as observed in the bulk structure [7] or due to the modulation of the lattice parameter of perovskite PZT to such an extent that it matches well with underlying Pt substrate, thereby, reducing the activation energy for nucleation of perovskite [10].

Sr addition at the "A" site increased intensity ratio of (111)/(200) in comparison to 2%Zn addition, which shifts the peak intensities to the tetragonal side of MPB and hence explains the increase in dielectric constant. Influence of Y^{+3} addition to the Pb^{+2} site is shown in Equation 2.

$$Y_2O_3 + 2(Pb^{2+}{}_{Pb^{2+}})^x + (V_{O^{2-}})^{\cdot\cdot} = 2(Y^{3+}{}_{Pb^{2+}})^{\cdot} + (O^{2-}{}_{O^{2-}})^x + 2PbO \qquad (2)$$

Substitution of Pb^{+2} by Y^{+3} improved the fatigue resistance of the film by reducing oxygen vacancy concentration. Y^{+3} by itself does not seem to be really promising because of relatively lower polarization and dielectric constant values. This is due to large size difference between available Pb^{+2} site and Y^{+3} cation size, 119 and 90 pm, respectively. This size difference is expected to create distortion in the cell so as to reduce the c/a value, thereby, reducing the ferroelectric properties. More characterization is needed to support this, since sufficient information is not available in the present literature. Due to the small size difference between Zn^{+2} and Zr^{+4}, 74 and 72 pm, and Sr^{+2} and Pb^{+2}, 112 and 119 pm, respectively, the lattice distortion effect is not that dominant for these two substitutions. We were able to achieve superior properties using PZT (52/48) with 2% Zn + 2% Sr. The combined effect of the two dopants seems to partially annihilate the effect of vacancies created by zinc addition and also attain a compromise in the dielectric constant and ferroelectric values. Since individually, Zn and Sr showed an improvement in Pr and Ps values, the combined polarization properties are even higher,

which is by far one of the highest reported values for a PZT based thin film. Currently pMUTs are being made with these films to test device efficiency.

2.5 Conclusions

Sr, Zn and Y doped perovskite PZT thin film were prepared by sol-gel method and characterized for their polarization values, dielectric constant and ferroelectric fatigue response for potential application in pMUTs. Properties with individual cations were first established and then properties were optimized using different combination of ions. Zn and Sr doped PZT films showed an improvement in the polarization values, but Y doped films showed better resistance to ferroelectric fatigue with lower polarization values. Significantly high values for saturation and remnant polarization, 108 $\mu C/cm^2$ and 54 $\mu C/cm^2$ respectively, were achieved with 2%Zn + 2%Sr 52/48 PZT.

Acknowledgement

Authors would like to acknowledge financial support from the Office of Naval Research under the grant N00014- 04-1-0644.

2.6 References

1. F. Akasheh, J. D. Fraser, S. Bose and A. Bandyopadhyay, "pMUTs: Modeling the Influence of Structural Parameters on Device Performance," *IEEE Transactions on Ultrasonics, Ferroelectrics and Frequency Control*, **52** [3], pp. 455-68 (2005).
2. F. Akasheh, T. Myers, J. D. Fraser, S. Bose and A. Bandyopadhyay, "Development of pMUTs," *Sensors and Actuators A*, **111** [2-3], pp.275-287 (2004).
3. B. Jaffe, W.R. Cook and H. Jaffe, "Piezoelectric Ceramics" *Academic Press, London* (1971).

4. G. H. Haertling, "Ferroelectric ceramics: History and technology," *Journal of American Ceramic Society* **82**, pp. 797-818 (1999).

5. Q. Zhang and R. W. Whatmore, "Improved ferroelectric and pyroelectric properties in Mn-doped lead zirconate titanate thin films," *Journal of Applied Physics* **94,** p 8 (2003).

6. W. S. Kim, S.M. Ha, H.H. Park and C.E. Kim, "The effects of cation substitution on the ferroelectric properties of sol-gel derived PZT thin films for FRAM application," *Thin Solid Films* **355-256**, pp. 531-535 (1999).

7. (a) A. Banerjee and S. Bose, "Nanocrystalline lead zirconate titanate using citrate nitrate autocombustion method: Low temperature synthesis and densification study", *Chem. Mater*., Volume 16, (26), pp 5610-5615 (2004); (b) A. Banerjee, A. Bandyopadhyay and S. Bose, "Effect of ZnO doping in PZT nanopowders," *Ceramic Transactions (CT) 159, p. 47.* Ceramic Nanomaterials and Nanotechnology III (2004).

8. S. Aggarwal and R. Ramesh, "Point defect chemistry of metal oxide hetrostructure", *Annual Review Matreial Science*, Volume 28, p. 463-99 (1998).

9. B.A. Tuttle, D.H. Doughty, R.W. Schwartz, T.J. Garino, S.L. Martinez et al., "Chemically prepared PZT film with Nb addition", *Ceramic Transaction,* Volume 15, p. 179-91 (1990).

10. Z. Huang, Q. Zhang and R.W. Whatmore, "Low temperature crystallization of lead zirconate titanate thin films by a sol-gel method," *Journal of Applied Physics* **85**, p 10 (1999).

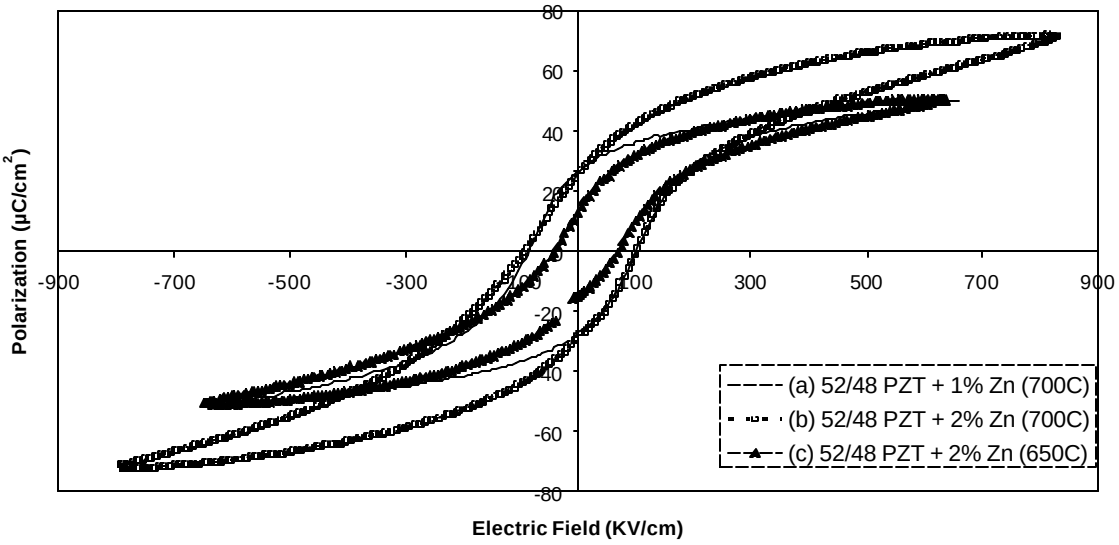

Figure 2.1 Polarization vs. electric field behavior for Zn doped PZT. (a) 52/48 PZT with 1-mol% Zn sintered at 700^0C, (b) 52/48 PZT with 2-mol % Zn sintered at 700^0C (c) 52/48 with 2-mol% Zn at sintered at 650^0C.

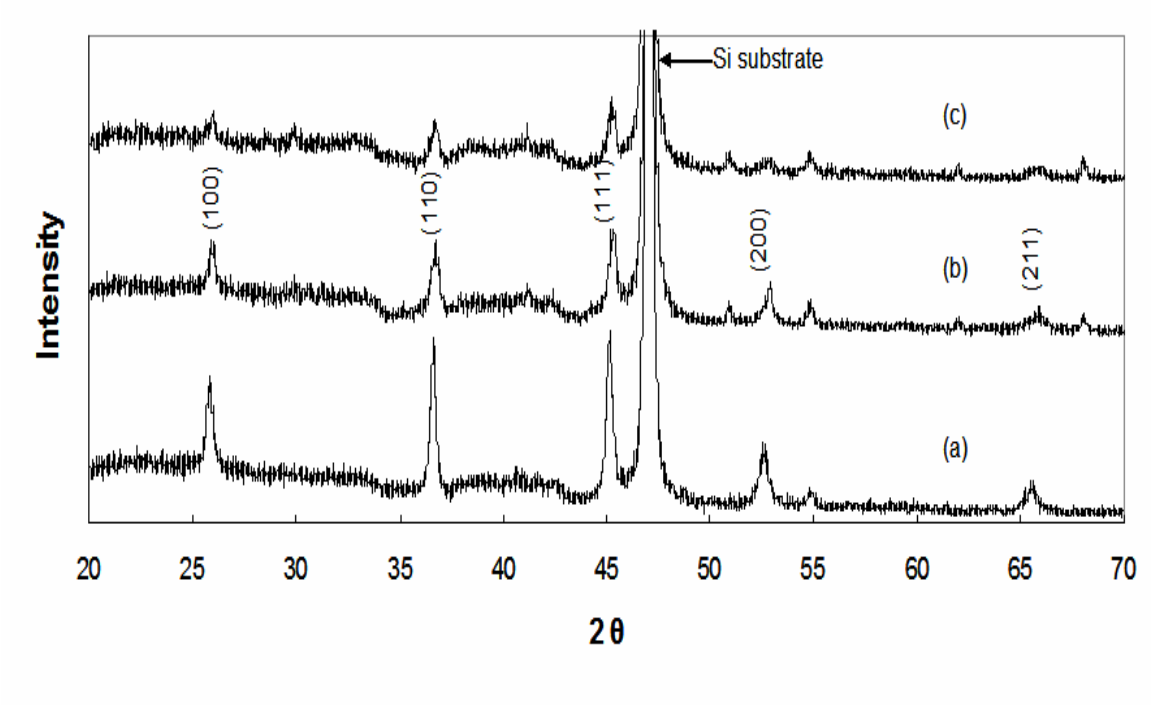

Figure 2.2 XRD patterns for doped PZT thin films. (a) 52/48 PZT with 2-mol% Sr addition, sintered at 700^0C; (b) 52/48 PZT with 2-mol% Zn addition, sintered at 700^0C; (c) 52/48 PZT with 2-mol% Zn addition, sintered at 650^0C.

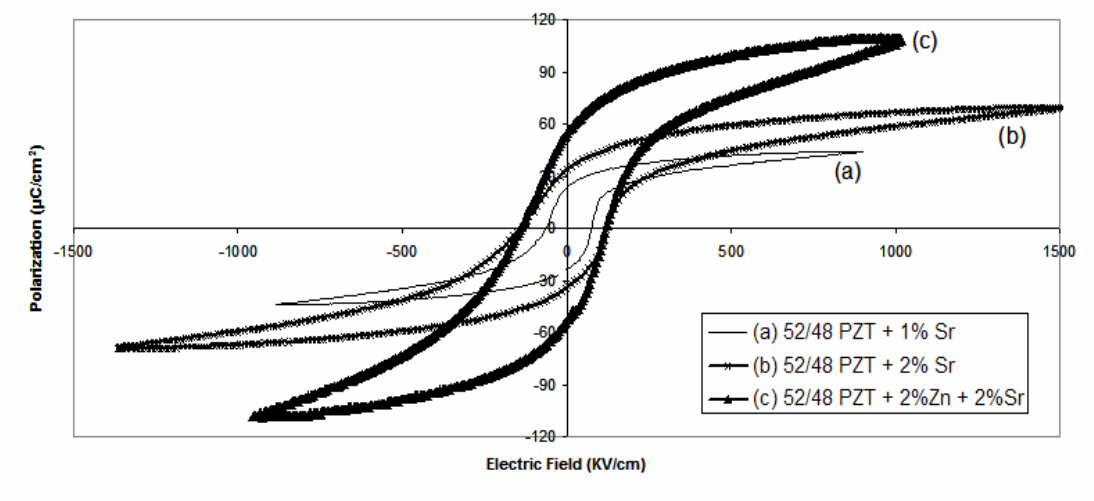

Figure 2.3 Polarization vs. electric field behavior for films sintered at 700^0C. (a) 52/48 PZT with 1-mol % Sr, (b) 52/48 PZT with 2-mol % Sr, (c) 52/48 PZT with 2-mol % Sr + 2-mol % Zn.

Compositions	Saturation Polarization ($\mu C/cm^2$) P_s	Remnant Polarization ($\mu C/cm^2$) P_r	Coercive Field (KV/cm) E	Dielectric Constant ε	Normalized remnant polarization after 10^8 cycles P_{nr}	Normalized remnant polarization after 10^9 cycles P_{nr}
52/48	47	24	110	3026	63%	22%
52/48 + 1%Zn	50	27	100	4400	15%	15%
52/48 + 2%Zn	72	27	100	3800	10%	10%
52/48 + 1%Sr	44	23	62	6166	62%	25%
52/48 + 2%Sr	69	33	136	6200	65%	36%
52/48 + 2%Y	40	26	160	2100	78%	75%
52/48 + (2%Zn, 2%Sr)	108	54	121	5000	55%	32%
52/48 + (2%Sr, 2%Y)	37	18	90	2960	74%	70%
52/48 + (2%Y, 2%Zn)	43	21	140	2830	58%	30%
40/60 + (2%Zn, 2%Sr)	66	32	102	3390	55%	32%
60/40 + (2%Zn, 2%Sr)	86	47	141	4280	55%	32%

Table 2.1: Ferroelectric properties for various Zn, Sr and Y doped PZT thin films sintered at 700^0C for 15 minutes.

Metal cation	Ti^{+4}	Zr^{+4}	Pb^{+2}	Zn^{+2}	Sr^{+2}	Y^{+3}
Ionic Radius (pm)	60.5	72	119	74	112	90

Table 2.2: Ionic radius of the substituting and parent cations.

CHAPTER THREE

INFLUENCE OF TOP ELECTRODE DESIGN ON pMUTs PERFORMANCE

3.1 Abstract

Piezoelectric micromachined ultrasonic transducers (pMUTs) were designed, fabricated and tested to measure resonance frequency and coupling coefficient. Prior to this, doped PZT thin film deposited on the membrane was tested for polarization values and later on for their ferroelectric fatigue resistance. Two different designs, single electrode and double electrode pMUT element, X and Y, respectively, were analyzed to understand the influence of design parameters on the device performance. Variation in the resonance frequency and efficiency of the device was investigated due to changes in the membrane dimension and top gold electrode design (gap and width), to have the ability to tailor the device. It was found that frequency decreases with increase in the membrane size for both the designs. Expanding gold electrode beyond the membrane dimension has a positive effect on the coupling coefficient of the pMUT elements. A gap of 20μm showed better efficiency than 30μm gap for the two electrode design.

3.2 Introduction

Miniaturization of electronic components have created interest in thin films as against to the commonly used bulk ceramic materials. Geometrical flexibility and easy integration to various devices has further accelerated its rapid growth both among the research and industrial community. Sensing and actuation capabilities in most of the MEMS devices utilize piezoelectric effect as in sonar systems [1], pressure sensors [2], ultrasonic transducers [3], accelerometers [4], controlling microfluidic flows in inkjet printer heads and others. Lead zirconate titanate (PZT) based piezoelectric material have

emerged as a material of choice due to excellent polarization values, dielectric constant, piezoelectric constant and thermal stability.

There are two types of MUTs: (1) cMUTs and (2) pMUTs. cMUTs uses a capacitive film, while pMUTs uses a piezoelectric actuated membrane to operate the device. Since its advent, these two working principles have kept competing with each other as the piezoelectric transducers [5-6] and the capacitive transducers [7], however, the high bias voltage which causes frequent collapse of the cMUTS [8] and complexity of having different designs for sending and receiving signals [9] has limited its universal acceptance.

This research investigates measures to improve properties of piezoelectric micromachined ultrasonic transducers (pMUTs) for medical imaging. The main thrust for this work can be defined as the need for transducer with inherently higher bandwidth, high sensitivity and better coupling coefficient with improved control over the resonance frequency. Such devices can find application in forward looking endoscopes, which have dimensions almost similar to that of the probe of the endoscope. Another area attracting wide attention is the fabrication of two-dimensional arrays of the single transducer [10] to obtain 3-D imaging of object such as moving heart. This would require complex signal processing and image development along with accurate working knowledge with single transducer and ability to put them in arrays. Improvement in pMUTs performance can be achieved through optimization in material and design variables. Research work focusing on material optimization [11] and FEA analysis [12] reported previously by our group has helped us to narrow down with respect to various ranges for different parameters regarding the designing of pMUTs.

3.2a Optimization Criteria

Using piezoelectric actuation, different frequencies can be generated via thickness and bending mode vibrations. However, limitation in the frequency range for medical imaging as 2-12 MHz excludes the use of thickness mode vibrations which normally results in frequency of GHz range for thin films [13]. The flexural mode of vibration i.e., k_{31} is used for generating desired frequencies as shown in figure 3.1, wherein, electric field is applied across the thickness, the 3 direction and longitudinal strains are generated along the 1 direction, which causes the membranes to vibrate along the direction of the applied field. The parameters that were studied are: (1) vibrating membrane width, (2) top gold electrode design and (3) effective area of membrane covered by the electrode. Influences of these parameters were studied based on their effect on resonance frequency and coupling coefficient of the pMUTs.

3.3 Experimental

3.3a pMUTs Designs

Figure 3.2 shows structural details of two different designs with the corresponding geometrical design parameters, which were investigated in this research. For the future discussion these will be referred as X and Y, wherein, X is a single electrode design and Y is a double electrode pMUT element. Starting with the first design, the single electrode (X), we simultaneously varied membrane width and top gold electrode as shown in Table 3.1. Corresponding to each membrane width, four electrode widths were studied. The length of these membranes is expected not to have a great impact on the properties provided they are at least in the ratio of 1:10 as width to length. Therefore, length (l) for 30, 60 and 90µm wide membrane were maintained at 1000µm and for 120µm wide

membrane at 1200µm. Gold electrode length (h) was also taken as a constant as, 900µm for 30, 60 and 90µm membranes and 1100µm for 1200µm membranes.

For the second design, the two electrode designs (Y), the parameters to evaluate are width of the membrane (w), gap between the electrodes (g) and width of the electrode outside/inside (+/-) the membrane (s). Vibrating membrane width was varied as 30, 60, 90 and 120µm. Two different values for 's' were tried as (+)10µm and (-)10µm along with 'g' values as 20µm and 30µm. 's' value of (+)10 corresponds to gold electrode extending 10µm beyond the membrane dimension and (-10) signifies gold electrode 10µm inside the edge of the membrane. Details of the designs studied are shown in Table 3.2. The designs for back-side membrane by Si etching and top gold electrode design were made using Corel-draw software and are shown in Figure 3.3a and 3.3b.

3.3b Fabrication of Membrane

Single side polished, p-type <100> silicon wafers with 74mm diameter and 380 +/-20µm thickness were used for the device fabrication. Process details for the membrane fabrication are shown in Figure 3.4. The wafers were subjected to high temperature wet oxidation at 1050^0C in oxygen and nitrogen environment. A 45 minutes ramp to 1050^0C was followed by 80 minutes soak time to grow a 300nm oxide layer on silicon. Nitrogen is maintained at 0.5 liters per minute throughout the process and oxygen at 3 liters per minute during the 80 minute soak period. Oxide on polished side of the wafer was then stripped using a buffered oxide etchant (BOE) consisting of (10:1) HF and NH_4F for 15 minutes, while the other side was protected using a semiconductor tape. This was followed by boron diffusion on the bare silicon side at 1125^0C for 110 minutes to result in approximately 2.3µm boron depth. The oxide layer on the back side prevents boron to

diffuse onto this side. Boron diffusion results in a borosilicate glass on the surface which needs to be stripped of to reduce the stresses in the wafer when platinum, PZT and gold layers will be deposited. This was achieved by a 20 minutes etching in BOE 10:1, followed by growing a sacrificial low temperature oxide (LTO) at 850^0C for two hrs. The LTO is then removed to ensure complete removal of boron skin and a second LTO is grown, which acts as an etch stop for silicon etch and a barrier between piezoelectric layer and conductive silicon wafer. Dimensions of the opening on the mask for back side etching to fabricate membrane on the polished side were significantly bigger than actual membrane size. These were calculated considering the 54.7^0 angle between the (100) and (111) etching directions and 380µm thickness of the silicon wafers.

Positive photolithography using AZ400K as photoresist was carried out to create oxide mask on back side of the wafer. The exposed silicon was then etched away using ethylenediamine pyrocatechol (EDP) at 110^0C for 4.5 hrs. This back-side etching resulted in 2µm thickness of silicon membrane of desired dimensions. Figure 3.5a shows an FESEM image of the back side of the membrane. The process was repeated for each wafer to create silicon membrane of different sizes to fabricate pMUTs.

3.3c PZT and Gold Electrode Deposition

Ti/Pt was sputter coated as 20nm Ti and 175nm Pt as bottom electrode on back side etched silicon wafers prior to PZT deposition. This was followed by a 10 minute annealing at 650^0C to relieve the strain energy associated with the residual stress development during sputtering [13-14]. 52/48 PZT + 2%Zn + 2%Sr was used as the precursor solution to be deposited on the platinized membrane. 0.5M metallorganic precursor solution were prepared via sol-gel method using 2-methoxy ethanol as a solvent

and lead acetate tri-hydrate, titanium isopropoxide (97%), zirconium n-propoxide (70% w/w in propanol), strontium isopropoxide (97%) and zinc acetate as the starting materials. Stoichiometric amount of lead acetate tri-hydrate and zinc acetate were dissolved in 2MOE. 10-mol% excess lead was added to this solution to compensate for the lead-loss due to volatization during sintering. This solution was distilled at 125^0C for 2h to remove the water of crystallization. Zirconium n-propoxide and titanium isopropoxide were then added along with the dopant strontium isopropoxide in a moisture controlled glove box, in desired amount to the above distilled solution. The solution was then refluxed at 125^0C for 5hrs to achieve a homogeneous precursor solution.

The precursor solution was spin coated on platinized silicon membranes at 4000 rpm for 12 sec. After each layer, the film was heated for 5 minutes separately on hot plates maintained at 125^0C and 325^0C. This process was repeated up to four layers. Final sintering was then carried out in a furnace maintained at 700^0C for 15 minutes. In the case of eight layer films, intermediate sintering at 600^0C for 15 minutes was carried out after four layers, before depositing another four-layer film sequence, followed by a final sintering at 700^0C for 15 minutes.

For top electrode, Ti/W was first sputtered for 17 seconds at 100W and 7.5mTorr and then Au sputtering was carried out for 15 minutes and 28 seconds at 75 W and 7.5mTorr. This resulted in 12.5nm of Ti/W as adhesive layer and 200nm of Au layer as top electrode. In order to pattern the top electrode, positive photolithography with AZ400K (photoresist) was used after careful alignment with the help of six poked holes in the wafer. Exposed gold was then etched away using Type TFA gold etchant for 2 minutes and Ti/W layer was removed using 30% hydrogen peroxide in water for 40

seconds. Figure 3.5b shows the FESEM pictures of the cross-section of the final device. The pictures does not resolves different layers of silicon, platinum, PZT and gold but gives an idea of approximate thickness ~ 400μm, of the final devices

3.4 Results and Discussion

The preliminary characterization of the devices was achieved by measuring ferroelectric properties using Precision workstation ferroelectric tester (Radiant Technologies, NM). Values obtained corresponding to designs X and Y are tabulated in Table 3.1 and Table 3.2, respectively. Results were uniform for different designs and ascertained the quality of the deposited PZT thin film. Figure 3.6a shows the polarization behavior of the deposited doped PZT material on the membrane. Precision Impedance Analyzer, Agilent Model 4294A was used for measuring resonance (f_r) and anti-resonance frequency (f_a). These values were then used to determine the coupling coefficient of the device using the relation

$$\frac{k^2}{1-k^2} = \frac{f_a{}^2 - f_r{}^2}{f_r{}^2} \qquad (1)$$

A D.C. voltage of 20V across the 0.6μm thickness of PZT film was applied during property measurement to pole the material, so as to visualize the capacitive-inductive transition in the device. Finally, films were tested for ferroelectric fatigue degradation under an applied A.C. field at 1MHz and 3V. PZT film retained 30% of remnant polarization after 10^9 cycles and the corresponding ferroelectric fatigue graph is shown in Figure 3.6b.

3.4a Design X:

The single electrode arrangement, design X, was investigated to understand the influence of membrane and top gold electrode width, as the main design parameters on

the resonance frequency and coupling coefficient. For this reason, membrane width was varied as 30, 60, 90 and 120µm along with the simultaneous variation in the dimension of top gold electrode, so that it stretches across the membrane width. Table 3.1 tabulates the results obtained corresponding to different variations in design X.

Figure 3.7a shows the effect of membrane and top gold electrode width on the resonance frequency. The x-axis contains gold electrode width with respect to membrane dimension and varies from (-) 10 to (+) 30µm i.e. the 's' value as explained previously. For a membrane of 90µm width, value corresponding to (-) 10µm in the figure 3.7a implies a gold electrode width of 90-10 = 80µm. As can be seen from graph, the resonance frequency is dependent on the membrane width to a greater extent than on the gold electrode width. It decreases as the membrane width increases from 30, 60, 90 and 120µm. For example, the resonance frequency values corresponding to (+) 10µm configuration of top electrode, i.e. 20, 50 , 80 and 110µm gold electrode width for 30, 60, 90 and 120µm membranes decreases from 2.023, 1.529 and 1.317 to 0.959, respectively. Moreover, for a given membrane dimension, resonance frequency increases with increase in top gold electrode width, but again this dependence is comparatively less than on membrane dimension.

The decrease in the resonance frequency with increase in the membrane width is reasonable and can be explained. As the width of the vibrating membrane is increased, it causes an increase in the wavelength generated by this membrane. There are no direct equations to show this relation, as would have been in the case of frequencies generated due to thickness mode vibration. With the velocity of the wave remaining same inside the material, this increase in wavelength causes a decrease in frequency with increase in

membrane width. Another reason for this is the increase in the mass of the vibrating membrane along with the platinum, PZT and gold layers on top of it with an increase in membrane width. This increase in the mass causes the overall frequency of the device to decrease. Also, a narrow membrane is expected to experience a higher restoring force as compared to a wider membrane due to increased stiffness which causes the resonance frequency to increase in the case of membrane with smaller width.

Figure 3.7b shows the effect on the coupling coefficient of the device due to design parameters. It has four different curves corresponding to different membrane dimensions. The efficiency showed a greater dependence on the top gold electrode dimension as against to membrane width. It increases as the gold electrode stretches beyond the membrane width and then decreases. For example, in the case of 120µm membrane, the coupling coefficient value increased from 1.44 to 2.52%, which corresponds to an increase of roughly 75%, as the gold electrode width increases from 80 to 100µm, i.e., from (-10) to (+10) in the Figure 3.7b and then decreased. A similar trend was observed with 30, 60 and 90µm membranes with the coupling coefficient value increasing by 43%, 40% and 36%, respectively, as the top gold electrode width was varied in the similar fashion.

If the top gold electrode width is less than the membrane dimension, such that it lies within the membrane, then on applying an electric field the center of the membrane and the position where top electrode is ending will have deflections in opposite direction. The end point of the top electrode will act as a hinge and will move in a direction opposite to the center of the membrane. Due to these complex vibrations present in the system, the membrane will not be able to achieve full deflection corresponding to an

applied electric field resulting in a decrease in the coupling coefficient values for such configuration. If the width of the top electrode is increased beyond the membrane dimension providing free movement, then the entire membrane will vibrate in the same direction, thereby, increasing the total deflection and hence efficiency. However, on increasing this top electrode width beyond a certain range, (+)10µm in this case, the extra electrode area will only add to the parasitic capacitance, instead of providing any useful mechanical vibrations and, therefore, the efficiency is expected to decrease. Figure 3.8 shows an example of resonance and anti-resonance frequency obtained using impedance analyzer for design X, with membrane width as 90µm and gold electrode width as 80µm.

3.4b Design Y:

For the double electrode design Y, performance of the device was evaluated as a function of membrane dimension, gold electrode width and the gap between these electrodes. For this purpose, membrane dimension was varied as 30, 60, 90 and 120µm. Two different electrode gaps were analyzed as 20 and 30µm (g = 20 or 30µm as shown in figure 3.2b) in combination with two separate positions for top electrodes, i.e., one 10µm inside the membrane and the other stretching 10µm outside the membrane. Resonance frequency and the corresponding efficiency obtained are tabulated in Table 3.2.

It is clear from the values in Table 3.2 that for a given membrane width, coupling coefficient is greater for top electrode extending outside the membrane dimension as compared to inside. For membrane dimension of 90 and 120µm, efficiency was higher for 's' values as (+) 10µm instead of (-) 10µm. Consider 120µm membrane with gap between the top electrodes as 20µm. The coupling coefficient value increased from 1.66% to 2.6% registering an increase of 56% and this increase was almost 175% in case of 90µm

membrane. This behavior with the double electrode design is in agreement to what we observed with single electrode design and strengthens our previous argument of increasing the deflections near the edge as one of the way to achieve higher efficiency.

Also, from Table 3.2, for a given membrane width and position of electrodes, i.e. either extending outside or inside, there was a decrease in efficiency with increase in the gap between the electrodes. A gap of 20µm gave better coupling coefficient values then 30µm gap. This is because a 30µm gap will lead to less active top electrode area on the membrane to provide the deflection. Gap effect on the efficiency can be better studied by varying it in a close interval in the range from 10µm to 30µm. However, for the present case 20µm gap shows a clear preference over 30µm gap in terms of efficiency, for example, in the case of 90µm membrane with 's' value as (+) 10µm, efficiency increased from 1.79% to 2.86%, as gap between the electrode decreased from 30µm to 20µm.

Except for a few anomalous values, resonance value showed a decrease with increase in membrane width. Another important notion to address over here would be comparatively large dependence of resonance frequency on the top electrode configuration for design Y then for design X. The resonance frequency is increasing with increase in gap between the electrodes. If we look at design Y with 60, 90 and 120µm membranes and (+) 10µm as the 's' value, the resonance value increases by 12%, 125% and observes a negligible decrease of 0.95%, respectively, as the gap between the electrode is increased from 20µm to 30µm. This frequency dependence due to top electrode design in case of double electrode pMUT element is much greater than in the case of design X, the single electrode pMUT.

After thoroughly investigating both the designs, it can be clearly stated that expanding top electrode beyond the membrane dimensions is favorable for the coupling coefficient values in both the cases. In the case of single electrode design, resonance frequency is mainly governed by the membrane dimension, however, in case of double electrode design it can be easily tailored both by membrane dimension and top electrode design. Coupling coefficient value in the case of single electrode was largely determined by the top electrode width; however, for double electrode design it can be controlled both by the gap and the width of the top gold electrodes. In brief it seems that in case of design Y, in spite of having efficiency in the same range as design X, it is much easier to tailor the resonance frequency and efficiency for a desired application.

4. Conclusion

Two different piezoelectric micromachined ultrasonic transducer designs using 52/48 PZT + (2%Zn+2%Sr) as active element were fabricated and tested for resonance frequency, coupling coefficient, polarization values and ferroelectric fatigue. The films showed saturation polarization of 56μC/cm^2, remnant of 26μC/cm^2 and retained 32% of remnant polarization after 10^9 cycles. Membrane width, top gold electrode dimension and the gap was varied so as to understand their individual effect on the performance of the device. In spite of the overall low efficiency of these membranes, we were able to establish critical design property relationships. For design X resonance frequency was primarily governed by the membrane dimension, instead of top gold electrode width and decreased with an increase in this value. Expanding the top gold electrode width 10μm beyond the membrane dimension increased the efficiency of the devices for both the designs. Resonance frequency for design Y was dependent both on membrane dimension

and top gold electrode design. A gap of 20µm for design Y showed better efficiency then 30µm gap.

3.6 References

1. J. J. Bernstein, L.C. Niles, H. Daniel Chen, L.E. Cross, K.K. Li and K. Udaykumar, Micromachined High Frequency Ferroelectric Sonar Transducers, IEEE Transactions on Ultrasonics, Ferroelectrics and Frequency Controls, Vol. 44, No. 5, Sptember 1997.

2. E. Defay, C. Millon, C. Mlhaire, D. Barbier, PZT Thin Films Integration for the Realization of a High Sensitivity Pressure Microsensor Based on a Vibrating Membrane, Sensors and Actuators, A 99 (2002) 64-67

3. H. Zhu, J. Miao, Z. Wang, C. Zhao, W. Zhu, Fabrication of Ultrasonic Arrays with 7µm PZT Thick Films as Ultrasonic Emitter for Object Detection in Air, Sensors and Actuators, Article in Press.

4. Y. Nemirovsky, A. Nemirovsky, P.Muralt and N. Setter, Design of a Novel Thin Film Piezoelectric Accelerometer, Sensors and Actuators A 56 (1996) 239-249.

5. F. Akasheh, T. Myers, J. D. Fraser, S. Bose and A. Bandyopadhyay, Developments of pMUTs , Sensors and Actuators A, 111 [2-3], pp 275-287 (2004).

6. J. Baborowski, N. Ledermann, P. Muralt, Piezoelectric Micromachined Transducers (PMUT's) Based on PZT Thin Films. Proceedings of the IEEE Ultrasonics Symposium (2002) – 1051

7. P.C. Eccardt, K. Niederer and B. Fischer, Micromachined Transducers for Ultrasound Application, Proceedings of the IEEE Ultrasonics Symposium (1997) – 1609

8. P.C. Eccardt and K. Niederer, Micromachined Ultrasonic Transducers with Improved Coupling Factors from a CMOS Compatible Process, Ultrasonics 38 (2000) 744.

9. I. Ladabaum, X. Jin, H.T. Soh, A. Atalar, Surface Micromachined Capacitive Ultrasonic Transducers, IEEE Transactions on Ultrasonics, Ferroelectrics and Frequency Control, Vol. 45, No. 3, (1998) 678.

10. G. Percin, A. Atalar, F.L. Degertekin and B.T.K. Yakub, Micromachined Two-dimensional Array Piezoelectrically Actuated Transducers, Applied Physics Letter, Vol. 72, No. 11, March 1998.

11. A. Dalakoti, A. Bandyopadhyay and S. Bose, Effect of Zn, Sr and Y addition on PZT Thin Films, Submitted to Journal of American Ceramic Society, 2005.

12. F. Akasheh, J. D. Fraser, S. Bose and A. Bandyopadhyay, pMUTs: Modeling the Effects of Structural Parameters on Device Performance, IEEE Transactions on Ultrasonics, Ferroelectrics and Frequency Control, 52[3], pp. 455-68 (2005)

13. A. Ehrlich, U. Weib, W. Hoyer and T. Gabner, Microstructural Changes of Pt/Ti Bi-layer During Annealing in Different Atmosphere – an XRD study, Thin Solid Films, 300 (1997) 122-130.

14. V. Branger, V. Pelosin, K.F. Badawi, Ph. Goudeau, Study of Mechanical and Microstructural State of Platinum Thin Films, Thin Solid Films 275 (1996) 22-24.

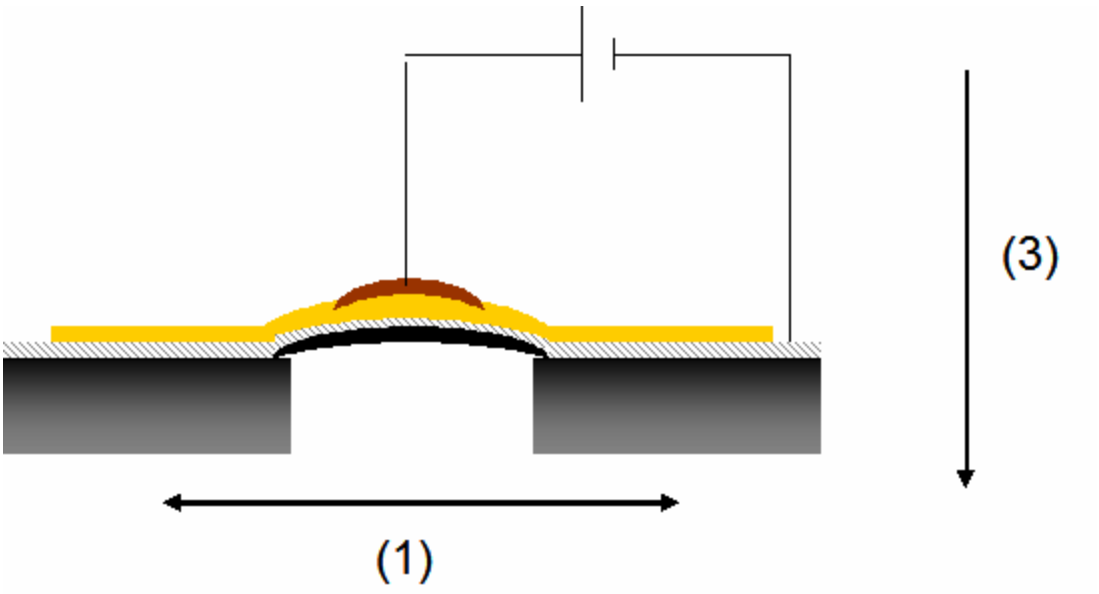

Figure 3.1: Flexural mode of vibration with (3) being the direction of applied electric field and (1) the direction of strains generated. Different layers from top are (a) Gold, (b) Doped PZT, (c) Platinum, (d) Boron doped silicon and (e) Silicon wafer.

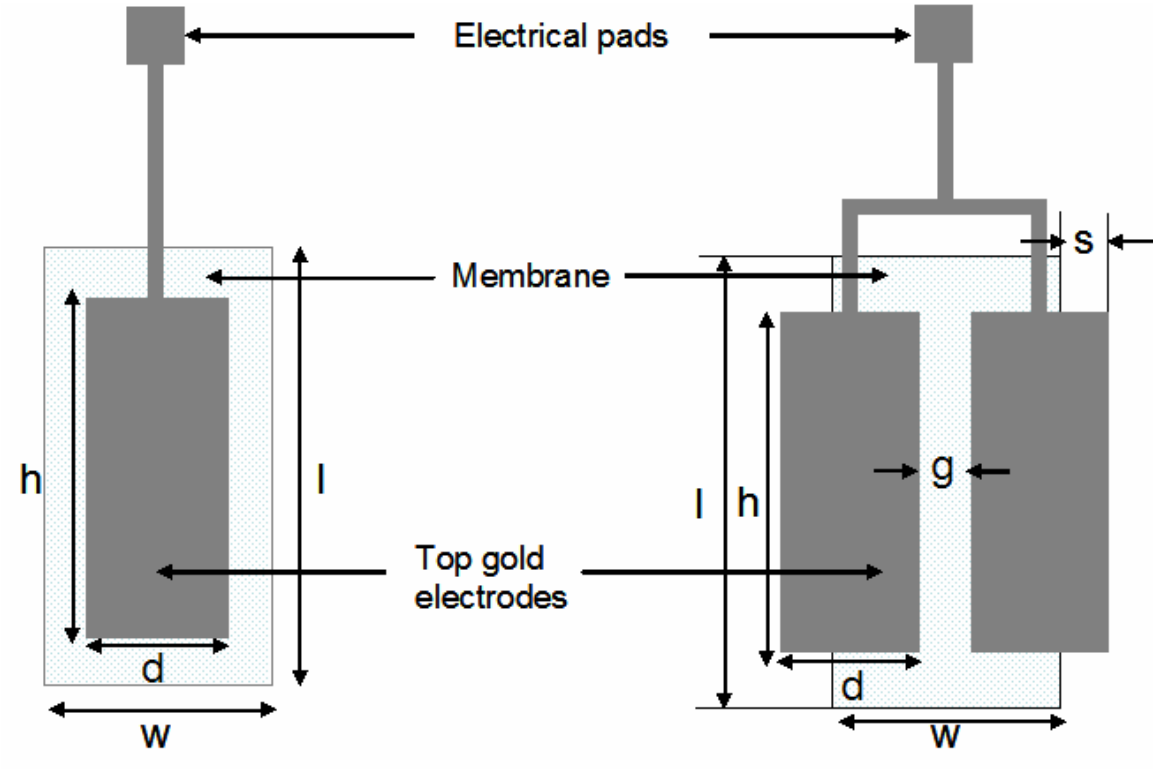

(a) (b)

Figure 3.2 Schematic details of design with respective variables. (a) Design X – Single electrode pMUT element. (b) Design Y – Double electrode pMUT element.

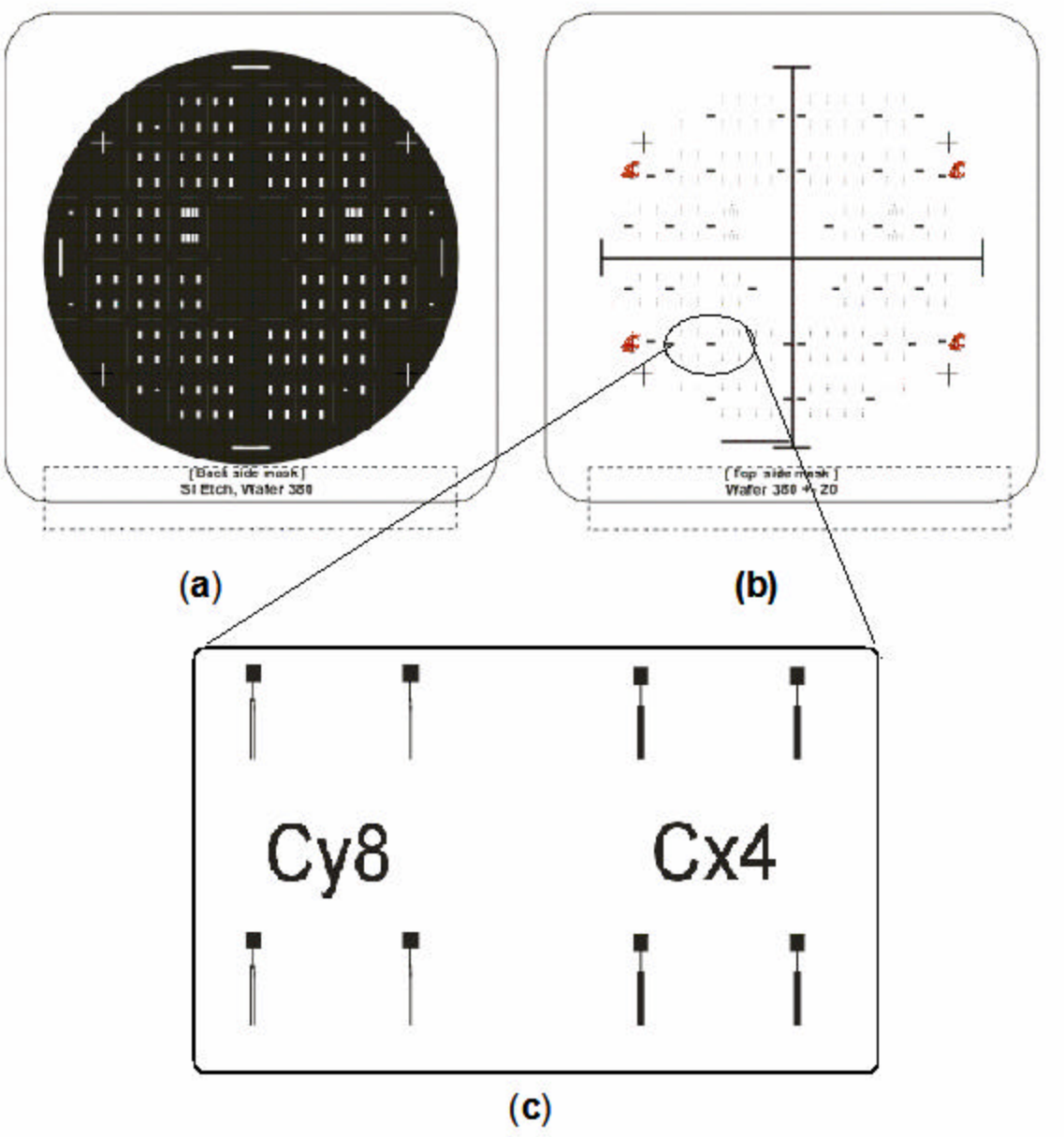

Figure 3.3 (a) Masks for back side etching (b) Mask for top gold electrode and (c) an enlarged image showing single (Cx4) and double electrode (Cy8) pMUT elements.

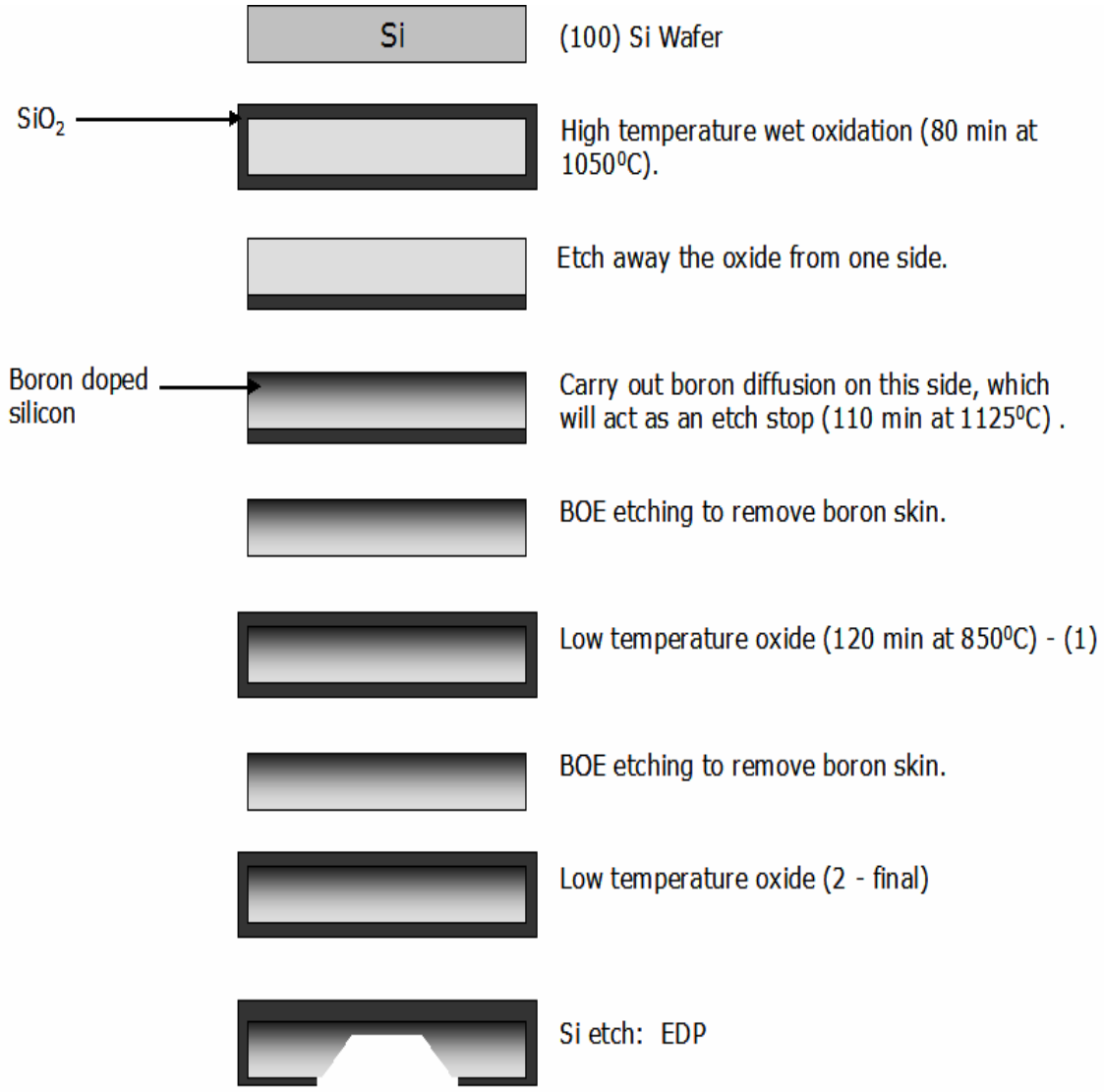

Figure 3.4 Silicon Membrane Fabrication.

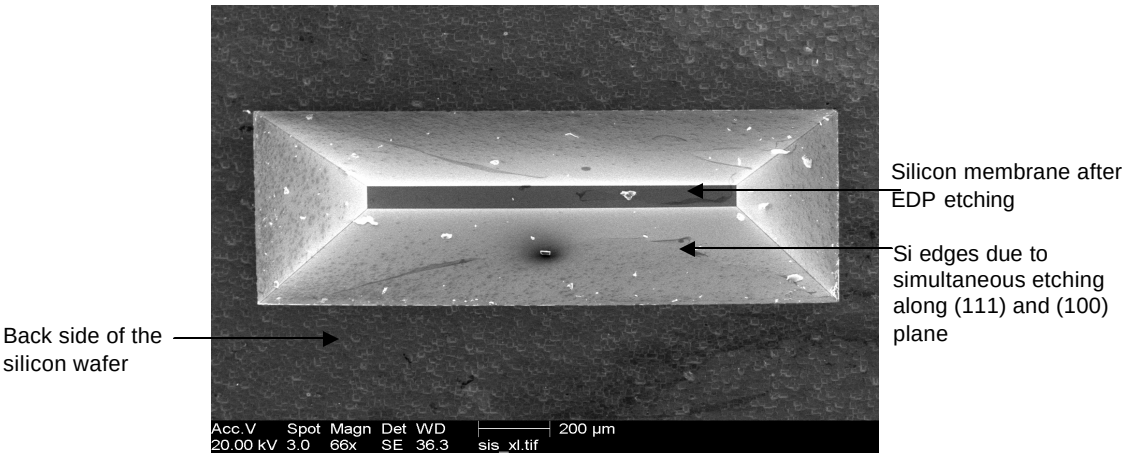

(a)

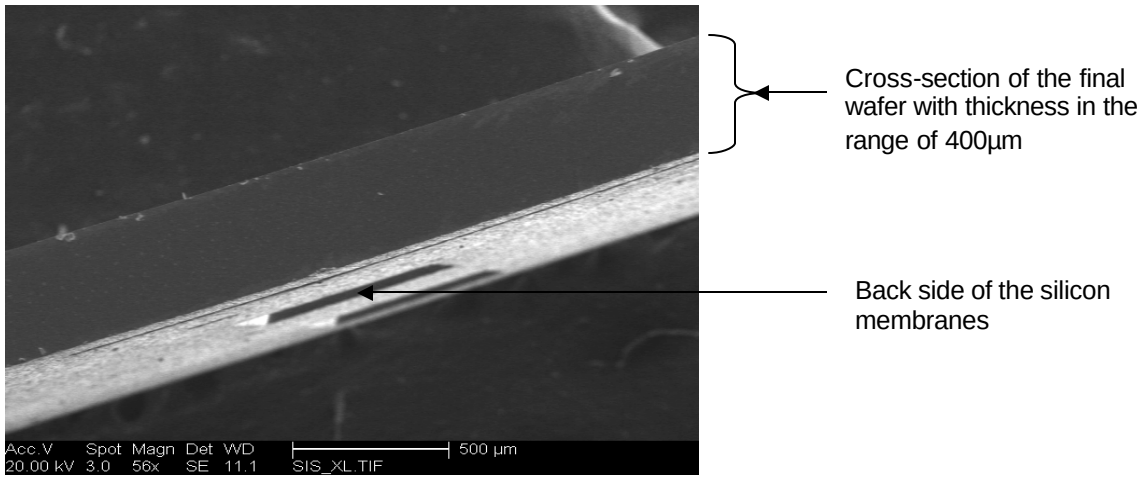

(b)

Figure 3.5 FESEM images of (a) Back side of the membrane after etching with EDP. (b) Cross-sectional view of the device after top gold electrode deposition at 56X.

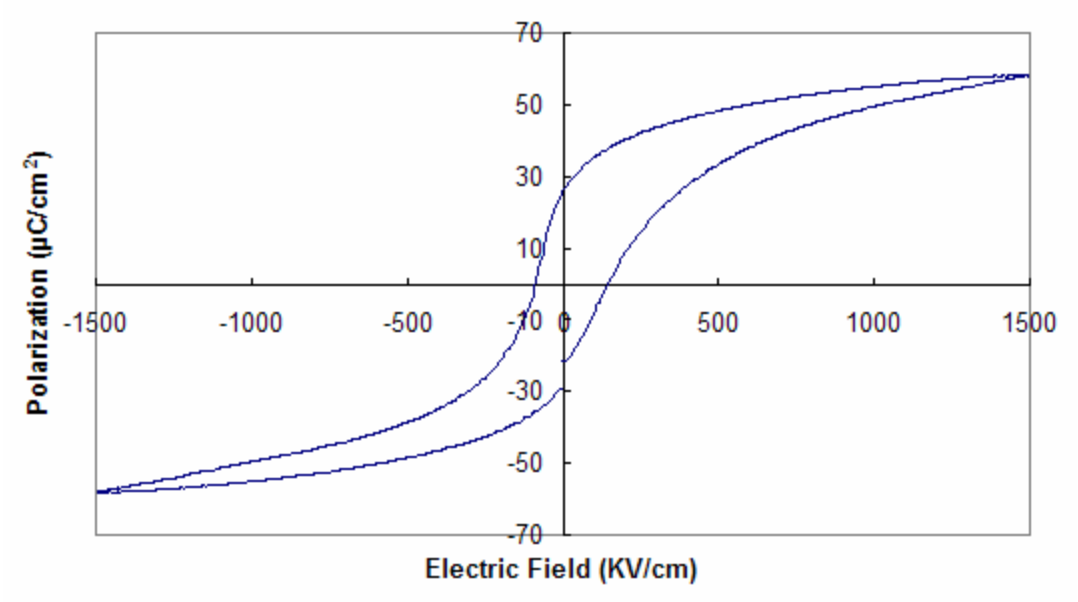

(a)

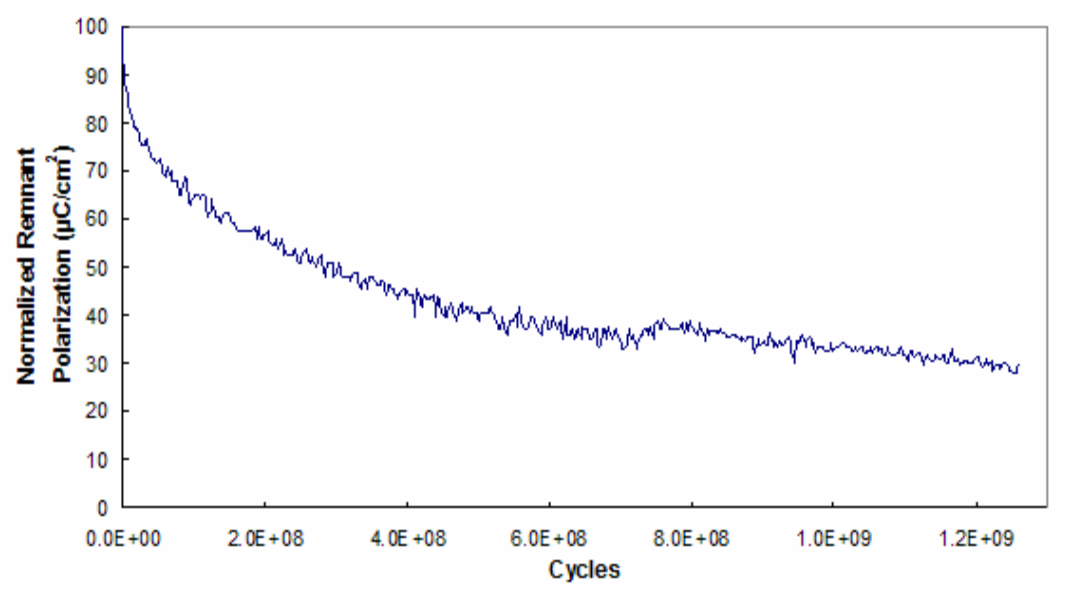

(b)

Figure 3.6 (a) Polarization behavior of the PZT film deposited on the membrane. (b) Fatigue response of the film after 10^9 cycles at 1MHz and 3V.

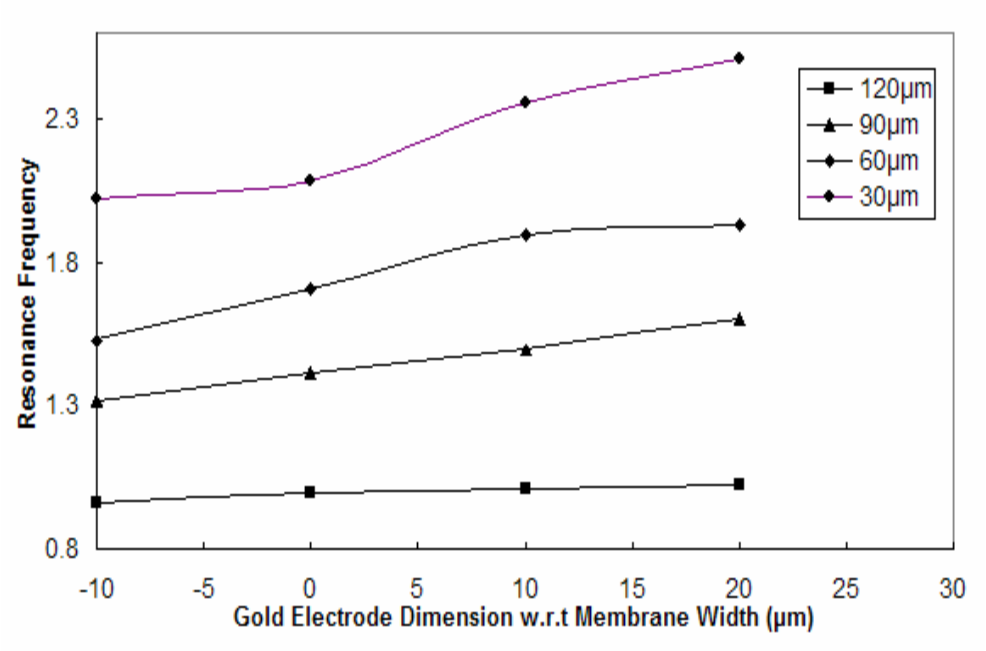

(a)

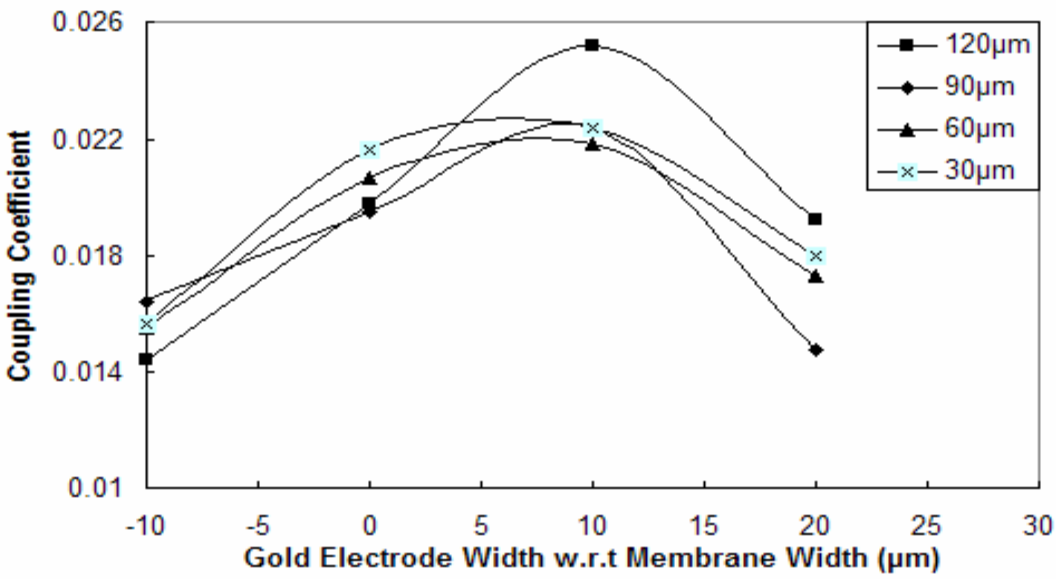

(b)

Figure 3.7 (a) Effect of membrane dimension and top gold electrode width on the resonance frequency for design X. (b) Effect of membrane dimension and top gold electrode width on the coupling coefficient of the device for design X.

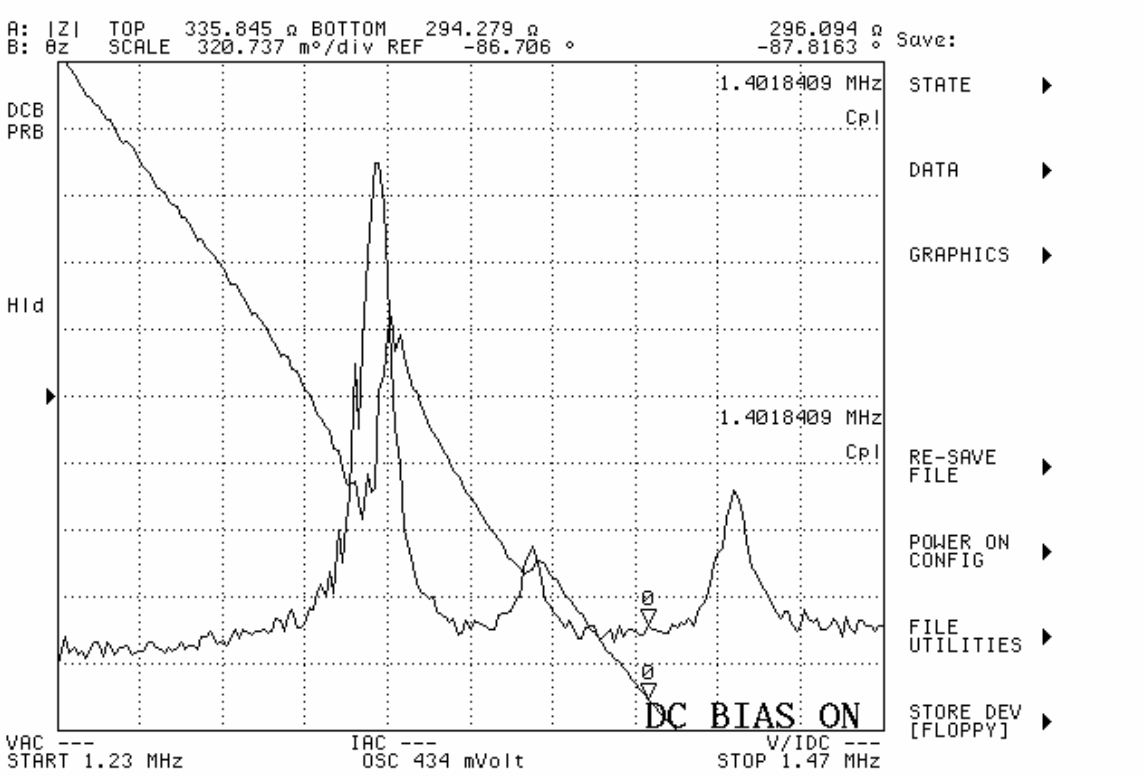

Figure 3.8 Variation in impedance (z) and phase angle (?) values with change in the frequency for design X corresponding to membrane width of 90µm and gold electrode width of 80µm.

Width of the membrane	*Top Gold Electrode Width*	*Resonance Frequency*	*Anti Resonance Frequency*	*Coupling Coefficient*	*Saturation Polarization*	*Remnant Polarization*	*Coercive Field*
(w) μm	*(d) μm*	*(fr) MHz*	*(fa) MHz*	*(k^2)*	*(Ps) μC/cm2*	*(Pr) μC/cm2*	*(Ec) KV/cm*
	110	0.959	0.966	0.0144	55.46	22.91	169.1
120	120	0.992	1.002	0.0198	55.59	22.814	171.01
	130	1.01	1.023	0.0252	56.05	22.47	149.61
	140	1.025	1.035	0.0192	56.67	22.269	132.41
	80	1.317	1.328	0.0164	55.41	23.75	178.38
90	90	1.412	1.426	0.0195	58.02	25.85	145.21
	100	1.492	1.509	0.0224	55.99	23.6	169.55
	110	1.607	1.619	0.0147	55.45	22.85	159.66
	50	1.529	1.541	0.0155	57.92	28.33	258.83
60	60	1.712	1.73	0.0207	56.5	27.01	261.66
	70	1.895	1.916	0.0218	57.06	27.43	255.75
	80	1.933	1.95	0.0173	56.47	27.08	259.16
	20	2.023	2.039	0.0156	54.4	26.79	322.7
30	30	2.089	2.112	0.0216	56.46	22.31	182.88
	40	2.36	2.387	0.0224	57.59	28.29	299.63
	50	2.511	2.534	0.018	56.24	26.61	264.4

Table 3.1. Frequency response using impedance analyzer and polarization values obtained corresponding to different variations in design X with 52/48 PZT + (2% Zn + 2% Sr) as the active element.

Width of the membrane	*Gap between the electrodes*	*Electrode outside/ inside the membrane*	*Resonance Frequency*	*Anti Resonance Frequency*	*Coupling Coefficient*	*Saturation Polarization*	*Remnant Polarization*	*Coercive Field*
(w) μm	*(g) μm*	*(s) μm*	*(fr) MHz*	*(fa) MHz*	*(k^2)*	*(Ps) μC/cm2*	*(Pr) μC/cm^2*	*(Ec) KV/cm*
120	20	(+) 10	1.054	1.068	0.026	61.62	25.01	187.85
	20	(-) 10	0.951	0.959	0.0166	63.48	28.24	218.08
	30	(+) 10	1.044	1.056	0.0225	58.54	26.03	230.9
	30	(-) 10	1.064	1.072	0.0148	63.26	26.4	177.91
90	20	(+) 10	1.707	1.732	0.0286	66.01	28.11	175.4
	20	(-) 10	1.523	1.531	0.0105	68.67	29.08	181.66
	30	(+) 10	3.846	3.881	0.0179	63.31	27.11	169.92
	30	(-) 10	1.669	1.68	0.013	63.54	27.4	189.13
60	20	(+) 10	2.683	2.709	0.0191	63.73	30.9	272.28
	30	(+) 10	3.01	3.025	0.0098	63.69	32.37	326.61
30	20	(+) 10	2.602	2.623	0.0159	71.38	30.13	192.31

Table 3.2. Frequency response using impedance analyzer and polarization values obtained corresponding to different variations in design Y with 52/48 PZT + (2% Zn + 2% Sr) as the active element.

CHAPTER FOUR

SUMMARY AND FUTURE PLAN

Development of better piezoelectric micromachined ultrasonic transducers was attempted in this project work. The problem was approached from both material and design point of view. Zinc, strontium and yttrium were the three dopant elements methodically selected to be used with 52/48 PZT for the first part of the research, wherein, improvement in the base active material of the device was attempted. Various compositions were characterized in terms of polarization values, dielectric constant, sintering temperature, electric field and ferroelectric fatigue. Effects of individual dopant element were first established. It was found that 2% Zn helps in reducing sintering temperature by 50^0C and increases the remnant and saturation polarization values. However, it deteriorates the resistance to fatigue for the deposited film. Strontium helped in improving the dielectric constant and polarization values, but increased the coercive field of the doped samples at the same time, making it difficult for dipoles to reorient. Yttrium showed tremendous improvement in the ferroelectric fatigue value and retained 75% of remnant polarization after 10^9 cycles, however, it decreased the polarization values. The composition was finally optimized as 52/48 PZT with 2% Zn + 2% Sr for further research regarding device fabrication.

Two different designs X and Y, single electrode and double electrode pMUT elements, respectively, were separately investigated to understand the effect of various design parameters as membrane dimension and top electrode design (width and gap between the electrodes) on the resonance frequency and coupling coefficient. Important property-dimension relations were established using the previously optimized PZT

solution, both for X and Y. It was found that resonance frequency was mainly governed by membrane dimension and decreases with increase in this value for both the designs. Expanding top gold electrode beyond the membrane size improved the coupling coefficient of the device. However, beyond 10µm, this value started decreasing due to increased capacitance introduced by top electrode, instead of providing any useful deflection to the membrane. For design Y, gap of 20µm showed better efficiency then 30µm.

It was finally established that in the case of single electrode design resonance frequency is mainly governed by the membrane dimension, however, in case of double electrode design it showed great dependence both on membrane dimension and top electrode design. Coupling coefficient value in the case of single electrode was largely determined by the top electrode width; however, for double electrode design it can be controlled both by the gap and the width of the top gold electrodes.

Further work in this area involves comparing the results obtained with standard PZT solution to illustrate the effect of better material on the overall properties. Over here we have used silicon wafers with thickness of 380+/-20µm. If we take into account the 54.7^0, the angle between (100) and (111) etching direction, we end up wasting a considerable amount of lateral length, thereby, increasing the overall device size. Using accurately diced 100µm thick wafers, polished on both the side can solve this problem and also help in fabricating focused transducer because of the easy flexibility of the thin wafer. Finally, after thoroughly understanding here the design effect on the single membrane, we can now further improve the efficiency and obtain 3D imaging by analyzing 1D and 2D arrays.

APPENDICES: WSU MICROFABRICATION RECIPIES

APPENDIX A: HIGH TEMPERATURE SILICON OXIDATION

1. Log HTO procedure into furnace logbook.
2. Put on nitrile glove.
3. Make sure you have a clear work area on the flow bench. Roll up vinyl curtain in front of the flow bench to allow access for when both of your hands are occupied.
4. Pour out the DI water in the oxygen bubbler flask heater, rinse out the flask with fresh DI water and fill the flask to the marked line with fresh DI water.
5. Turn on the power to the oxygen bubbler flask heater and verify that the heater control set point is at **93^0C**.
6. Put on hot glove.
7. Remove the end cap from the upper oxidation furnace.
8. Take off the hot glove.
9. Use the quartz rod to pull the oxidation wafer boat from the oxidation furnace on to the quartz wafer carrier and take it to the flow bench with the quartz wafer boat carrier.
10. Replace quartz rod.
11. Load the wafers in the boat, with the side to be boron doped facing the gas flow from the furnace. Place two dummy wafers at each end of the wafer arrangement.
12. Move the boat with wafer to the oxidation furnace (cold). Use the quartz rod to slide the boat to the center of the furnace.
13. Place the end cap. Check the furnace cooling water supply valve is open and the water supply line is cold.

14. Turn on over circuit breakers. Check the main nitrogen supply and adjust the rotimeter until the silver ball is at **55** or 3 liters per minute.
15. Turn on oxidation furnace temperature control switch. Wait for 10 seconds. Turn on oxidation furnace heating element switch.
16. Set the middle temperature switch **842**. This corresponds to a temperature of 1050^0C. Leave the right and left temperature switch at **500**.
17. Set the timer to t = 00:00:00
18. At t = 00:40:00, check the temperature on oxygen bubbler is 93^0C, oxidation furnace temperature is 1050^0C and main oxygen supply valve is on.
19. At t = 00:45:00, adjust oxygen flow rate to **3.2** or 0.5 liters per minute. Run the furnace for one hour twenty minutes.
20. At t = 02:05:00, Turn off oxygen supply and rotimeter valve. Turn off power supply to oxygen bubbler. Check nitrogen flow is still at **55** or 3 liters per minute. Remove the end cap from the furnace and begin 10 minute pull out of the wafer boat from the furnace at a rate of 1 inch every 30 seconds.
21. At t = 02:15:00, take the wafer boat to the flow bench to cool to handling temperature. Turn off oxidation heating element switch and temperature control switch.
22. Replace furnace end cap. After furnace has cooled to 300^0C, turn nitrogen down to just a trickle.

APPENDIX B: DRYING BORON WAFER

The purpose of this process is to dry the boron wafers that will be the source of boron for boron diffusion process.

1. Load the born disk into boron diffusion wafer boat.
2. Set oven temperature to **598** or 800^0C. Set nitrogen at **43**.
3. At t = 00:00:00, once the furnace has reached the operating temperature, open the end cap and begin the 10 minute push of the wafer boat into the furnace. Replace furnace cap.
4. At t = 00:40:00, remove the end cap and begin the 10 minute pull out of the wafer boat. Move it to flow bench and allow it to cool to room temperature.

During this 40 minute period, etch out one side of HTO prepared wafer to make it receptive to boron diffusion.

APPENDIX C: BOE SINGLE SIDE SILICON OXIDE ETCH

1. Cover back side with semiconductor tape, trim flush w/ edges.
2. Put in 10:1 BOE for 10 minutes to strip all oxide from exposed side.
3. Cycle 3x through DI dump rinse
4. Soak in acetone to remove semiconductor tape.
5. Rinse in IPA bath
6. Rinse in DI Bath
7. Spin dry with heated nitrogen

APPENDIX D: BORON DIFFUSION

1. Place wafer in boron wafer boat with etched side to receive boron, facing the boron disk. Between each set of boron disk, there will be two wafers facing the boron disk.
2. Furnace should be at **598** or 800^0C from the drying process.
3. Adjust oxygen flow rate to **9** or 1.5 liters per minute.
4. Adjust nitrogen flow rate to **27.5** or 1.5 liters per minute.
5. At t = 00:00:00, begin 10 minute push of wafer boat into the diffusion furnace.
6. At t = 00:10:00, close the end cap and allow the temperature to stabilize for 10 minutes.
7. At t = 00:20:00, begin 2 minute hydrogen injection, turn off nitrogen. Adjust H2N2 mix to **3.8**5 or 1.5 liters per minute.
8. At t = 00:22:00, turn off oxygen, turn off H2N2, turn on and adjust nitrogen to **55** or 3 liters per minute.
9. At t = 00:27:00, begin 10 minute temperature ramp to 900^0C by adjusting lower furnace temperature to **693** or 900^0C.
10. At t = 00:37:00, begin 10 minute oxidation, adjust oxygen flow rate to **2.5** or 0.3 liters per minute.
11. At t = 00:47:00, turn off oxygen, begin 21 minute ramp to 1125^0C by adjusting the oven temperature to **922**.
12. At t = 01:08:00, start 110 minute soak.

13. At t = 02:58:00, turn of heating element switch and temperature control switch. Allow it to cool to 750^0C for 25 minutes.
14. At t = 03:23:00, remove the end cap and begin 10 minute pull out of wafer boat.
15. At t = 03:33:00, turn off nitrogen, move the wafer boat to the flow bench and allow it to cool to room temperature.

APPENDIX E: LOW TEMPERATURE SILICON OXIDATION

Run a 20 minute BOE borosilicate etch prior to LTO. The purpose of this process is to grow a low temperature sacrificial silicon dioxide layer on the wafer. It will be stripped to remove impurities in the boron surface and provide a foundation for the final oxide layer.

1. At t = 00:00:00, verify furnace temperature is maintained at **642** or 850^0C and nitrogen flow is at **55** on the rotimeter. Begin 10 minute push of the wafer boat into the furnace.
2. At t = 00:03:00, set oxygen to **15** or 3 liters per minute. Turn off nitrogen and verify that oxygen bubbler is working.
3. At t = 00:10:00, replace oxygen furnace end cap and allow the furnace to run for two hours.
4. At t = 02:10:00, set nitrogen to **55** or 3 liters per minute. Turn off oxygen, turn off oxygen bubbler heater and begin 10 minute pull out of the wafer boat.
5. At t = 02:20:00, move the wafer boat to the flow bench. Allow it to cool to room temperature and go for 10 minute BOE sacrificial LTO etch.
6. Grow final LTO at the end of sacrificial etching.

APPENDIX F: AZ5214-EIR POSITIVE PHOTOLITHOGRAPHY (FOR OXIDE ETCH)

1. Turn on the mask aligner and allow at least 10 minutes for stabilizing. This is accomplished by turning the power switch to "on," and then pressing the start button after a few seconds.
2. Turn on the blue Cole-Parmer Digital hotplate and set to 110^0C. Allow at least 10 minutes for this to get up to temperature.
3. Spin HMDS prime:
    a. Center the wafer on spin coater chuck
    b. Test spin up to 3000 rpm. Set the timer for 30 seconds at 3000 rpm, with acceleration set to about the 11:00-12:00 position on the dial. The deceleration is not an important parameter and is typically set to about the 3:00 position on the dial so that it stops quickly.
    c. Use a plastic transfer pipette to deposit 1,1,1,6,6,6-hexamethyldisilazane (HMDS) onto wafer. It has a low surface tension, so a little goes a long ways. This is a very volatile and toxic liquid, and it should only be opened and dispensed in a fume hood. Because of the hygroscopic nature of the HMDS, it should be tightly capped as soon as possible to maintain its effectiveness for priming.
    d. Spin the HMDS at 3000 rpm for 30 seconds
4. Spin photoresist
    a. Use a plastic transfer pipette to deposit AZ5214 photoresist onto the wafer. Make sure that it goes nearly to the edge of the wafer.

b. Spin at 3000 rpm for 30 seconds

c. Softbake the photoresist for 60 seconds on a hotplate at 110^0C. (towards the back, right of center)

5. Align the wafer with desired mask and expose for 12 seconds.

6. Develop 60 seconds with agitation in 4:1 AZ400K (H_2O: developer). A solution of 12 mL:48 mL is adequate for developing one wafer, but it should be noted that the developer is consumed in a chemical reaction with the photoresist. Rinse with DI water and blow dry with canned air. Check that the photoresist has fully developed by visual inspection or with the stereo microscope.

7. Oxide Etch

   a. Tape the backside of the wafers with blue semiconductor tape, allowing an extra 1/8 inch around the edges. Wrap this extra tape over to the front side to protect the wafer edges from etching, carefully pressing it down with a fingernail or the back of wafer tongs.

   b. Etch in 10:1 Buffered Oxide Etch (BOE) for 5 minutes to expose silicon.

   c. Cycle 5x through DI dump rinse (alternate between two 3L plastic beakers using ~2L DI water, rinse beaker thoroughly with running DI water before refilling it)

   d. Remove semiconductor tape and rinse twice with acetone and IPA to remove photoresist.

   e. Blow dry the wafers with canned air.

APPENDIX G: EDP ETCHING FOR SILICON

Chemical required:

Catechol – 312gm

Pyrazine – 7.3 gm

Ethylenediamine – 975mL

DI water – 312mL

1. Add 312 g catechol and 7.3 g pyrazine to clean desiccator.
2. Measure out 312 mL DI water in a clean graduated cylinder. Add slowly to the desiccator; stir thoroughly with a glass rod.
3. Add 975 mL of ethylenediamine slowly to the mixture while stirring with a glass rod. This is an exothermic reaction and should be carried out slowly.
4. Stir all the chemicals with a glass rod and use a vacuum seal to close the desiccators.
5. Turn on water flow to the reflux condenser.
6. Turn on hot plate to maintain EDP temperature as 110^0C.
7. Introduce wafer using a wafer boat into the solution, once the temperature is stabilized.
8. Etch the wafer for four hours and thirty minute, take it out and examine for under etching. If yes, carry out the etching for another 15 minutes.
9. At the end of the process, lift the wafer boat out of EDP solution and immediately immerse it in DI water solution.
10. Rinse the wafer three times with fresh DI water. Finally clean the wafers with acetone IPA and DI. Blow air to get a clean surface.

APPENDIX H: TOP GOLD ELECTRODE ETCHING (POSITIVE PHOTOLITHOGRAPHY)

1. Spin HMDS prime:

   a) Center the wafer on spincoater chuck.

   b) Test spin up to 3000 RPM.

   c) Use a plastic transfer pipette to deposit HMDS onto wafer. It has a low surface tension, so a little goes a long ways.

   d) Spin the HMDS to 3000 RPM for 30 seconds.

2. Spin photoresist

   a) Use a plastic transfer pipette to deposit photoresist onto the wafer. Make sure that it goes nearly to the edge of the wafer.

   b) Spin to 3000 RPM for 30 seconds.

3. Softbake the photoresist for 60 seconds at 110^0C on a Cole-Parmer Digital hotplate.
4. Align the wafer with desired mask and expose for 12 seconds.
5. Develop 60 seconds with agitation in 4:1 AZ400K (H_2O: developer).
6. Rinse in DI water, carry out gold etching for 2 minutes with agitation in Transene Type TFA gold etchant.
7. Rinse in DI water, etch TiW for 40 seconds with agitation in 30% hydrogen peroxide.
8. Rinse in DI water, wash off the remaining photoresist with two acetone/IPA rinses.
9. Dry the wafer with canned air, and 3 minutes on a hotplate at ~120^0C.